Carbon 229 (2024) 119542

Contents lists available at ScienceDirect

Carbon

journal homepage: www.elsevier.com/locate/carbon

Facile synthesis of nano-si/graphite-carbon anode through microwave-induced carbothermal shock for lithium-ion batteries

Chang-Hyun Cho [a,b], Won Ung Jeong [a], Chang-Ha Lim [b], Jae-Kook Yoon [b], Chris Yeajoon Bon [b], Kap-Seung Yang [b,**], Min-Sik Park [a,*]

[a] Department of Advanced Materials Engineering for Information and Electronics, Integrated Education Institute for Frontier Science & Technology (BK21 Four), Kyung Hee University, 1732 Deogyeong-daero, Giheung-gu, Yongin, 17104, Republic of Korea

[b] Rechargeable Battery Composite Materials R&D Center, Deca Material Inc., 224 Wanjusadan 6-Ro, Bongdong-Eup, Wanju-Gun, Jeollabuk-Do, 55317, Republic of Korea

ARTICLE INFO

Keywords:
Graphite
Nano silicon
Carbothermal shock
Lithium-ion batteries
Anode materials

ABSTRACT

We present a cost-effective synthesis process for producing a carbon-coated nano-Si@Graphite (n-Si@G-C) anode, in which nano-sized Si (n-Si) particles (~50 nm in size) are anchored onto natural graphite particles by a carbothermal shock through microwave induction. During the carbothermal shock process, graphite undergoes a fast increase in temperature resulting in micron-sized Si (m-Si) particles (~4 μm in size) to undergo stress fractures due to rapid thermal expansion. This process leads to the formation of abundant n-Si particles onto graphite particles. Subsequently, a thin carbon shell is introduced by a wet-coating process combined with a thermal decomposition of coal-tar pitch. The amorphous carbon shell offers multiple functionalities: i) preventing direct exposure of n-Si particles to the electrolyte, ii) accommodating their volume expansion, and iii) maintaining electron conduction pathways. The resulting n-Si@G-C anode allows a high reversible capacity (500.8 mAh g^{-1}) as well as fast-charging characteristics. When utilized in a full-cell configured with a commercial-grade $LiNi_{0.8}Co_{0.1}Mn_{0.1}O_2$ cathode, it achieves a notable reduction in charging time (approximately 10.1 min@80 % state of charge). After 300 cycles, a high capacity retention (71.3 %) can be retained under 3C charging. Moreover, the distinctive structural features of the n-Si@G-C anode effectively suppress undesirable Li plating.

1. Introduction

To meet the growing demands of long-range electric vehicles, it is becoming exponentially important to enhance the energy density as well as lifespans of current lithium-ion batteries (LIBs). Therefore, the design and synthesis of advanced materials are essential for realizing lightweight, high-energy LIBs in emerging markets. Si-based composites have garnered considerable interest as promising candidates for advanced LIBs based on their abundance and the high theoretical capacity of Si ($Li_{15}Si_4$, 3580 mAh g^{-1}), in contrast to commercially available carbonaceous anodes (e.g. graphite and hard carbon) [1,2]. However, Si-based composites exhibit a rapid loss of reversible capacity through the alloying-dealloying process with Li^+ during cycling. It is because the severe volume variations of Si (~300 %) cause significant structural degradation, leading to unstable solid–electrolyte interphase (SEI) formation as well as electrical contact loss [3,4].

To address these technical challenges, various efforts have been directed toward reducing the particle size of Si and constructing composites with conductive materials with the purpose of advancing the electrochemical performance of Si-based composites [5]. Particularly, nano-sized Si (n-Si) particles dispersed within a conductive host are essential for accommodating the severe volume variations of Si while maintaining sufficient electrical conduction during cycling [6–14]. However, synthesizing high-quality n-Si particles remains a significant challenge in developing reliable Si-based composites due to the complexity of the synthesis process and high production costs. Thus, it is deemed necessary to design a facile, scalable, and cost-effective synthesis process for n-Si particles on a commercial scale.

Recently, numerous approaches have been explored to produce n-Si particles such as thermal evaporation [15,16], mechanical milling, and

* Corresponding author.
** Corresponding author.
E-mail addresses: ksyang@decamaterial.com (K.-S. Yang), mspark@khu.ac.kr (M.-S. Park).

https://doi.org/10.1016/j.carbon.2024.119542
Received 24 April 2024; Received in revised form 15 July 2024; Accepted 10 August 2024
Available online 10 August 2024

sol-gel reactions [17,18]. Yao et al. successfully synthesized high-entropy-alloy nanoparticles on the carbonized nanofiber web via a carbothermal shock by electro-conduction. In practice, various single-phase nanoparticles consisting of several atoms can be successfully obtained by flash Joule heating and cooling from a mixture of the metal salts loaded onto carbon supports (heating temperature and rate of ~2000 K and 105 K s^{-1}, respectively) [19]. On the other hand, the carbothermal shock process developed by Deca Material Inc. is one of the most promising synthetic routes in terms of uniformity and purity of the resulting n-Si particles with homogeneous dispersions on carbon materials [20]. In principle, the graphitic carbon materials contain highly mobile π-electrons in sp^2 hybridized C–C bonds. Si particles in contact with graphitic carbons can be thermally shocked through microwaved-induced heating of the graphite without electrode contact, or Joule heating through an applied current with electrode contact. The sudden increase in thermal energy facilitates the fracturing of Si from micro to nano-sized particles.

Inspired by these results, herein, we propose a robust design for a carbon-coated nano-Si@Graphite (n-Si@G-C) anode for use in LIBs. First of all, the nano-Si@Graphite (n-Si@G) composite was initially synthesized by the carbothermal shock process on a mixture of micron-sized Si (m-Si) and graphite [21]. After integrating n-Si particles onto the graphite surface, an amorphous carbon shell was introduced onto the n-Si@G composite through the thermal decomposition of coal-tar pitch. Our primary objectives in this materials design are twofold: i) to enhance the Li^+ storage capacity by integrating n-Si particles onto graphite, and ii) to mitigate the direct electrolyte contact of the n-Si particles while accommodating volume variations of the n-Si particles and preserving electron conduction pathways within the composite by utilizing an amorphous carbon shell. To examine the feasibility of the n-Si@G-C anode, its electrochemical performance was thoroughly examined in half and full-cell configurations coupled with a commercial cathode ($LiNi_{0.8}Co_{0.1}Mn_{0.1}O_2$), providing a comprehensive understanding of the reaction mechanism. This work offers practical insights into advanced materials design and cost-effective synthesis methods for mass-production of highly reliable Si-based anode for realizing advanced LIBs.

2. Experimental details

2.1. Synthesis of n-Si@G-C composite

Using a custom-made microwave equipment made by Deca Material Inc., microwave induction was applied to a mixture of m-Si and natural graphite as the starting materials for an efficient process, taking advantage of a non-contact method suitable for scale-up production [22–25], which eliminates the need for electrode contact. The m-Si (~4 μm in size) and graphite (~10 μm in size) were thoroughly mixed at a ratio of 1:9, respectively and loaded in a rectangular container, followed by carbothermal shock at a frequency of 2.45 GHz and at 3 kW for 40 s. After microwave irradiation, the m-Si particles were stress fractured due to rapid thermal expansion, and upon quenching, abundant n-Si particles were anchored onto the graphite surface. The n-Si@G composite (9.0 g) was stirred at 400 rpm with coal-tar pitch (1.0 g, Sigma-Aldrich) in tetrahydrofuran (THF, 40 ml, Sigma-Aldrich) solvent before drying at 80 °C. Following this, as-prepared powder underwent additional heating in a furnace under Ar flow at 1000 °C for 2 h. The resulting n-Si@G-C composite was ground and sieved before use.

2.2. Structural characterizations

Field-emission scanning electron microscopy (FESEM, JSM-7000F) was employed for morphological examination. Transmission electron microscopy (TEM, ARM-200F) and energy-dispersive X-ray spectroscopy (EDS) were used for microstructural investigations. Powder X-ray diffraction (XRD, Empyrean) and Raman spectroscopy (Raman, Olympus BX43) were utilized for examining structural characteristics. For surface analysis, X-ray photoelectron spectroscopy (XPS, K-alpha) was also employed. Electrical conductivity was measured using powder resistivity measurement systems (MCP-PD51). Thermogravimetric analysis (TGA, PerkinElmer) was conducted for compositional analyses. Additionally, particle size analysis was performed using a particle size analyzer (PSA, NPA252), and the Brunauer-Emmett-Teller (BET) surface area analyzer (Micromeritics Tristar 3020) was employed to examine structural features.

2.3. Electrochemical measurements

Both the anode and cathode were fabricated using active materials, together with Super-P (conducting agent) and PVDF (binder) through a conventional casting process. The anode slurry was prepared at a ratio of 90:5:5 and casted onto copper (Cu) foil (11 μm thick). Both loading level (4.3 mg cm^{-2}) and electrode density (1.5 g cm^{-3}) of the anodes were carefully controlled. On the other hand, the cathode slurry was formulated in a ratio of 96:2:2 and casted onto aluminum (Al) foil (15 μm thick). The cathodes also have controlled loading level (8.2 mg cm^{-2}) and electrode density (3.2 g cm^{-3}). In assembling the half-cell, a Li metal foil (200 μm thick, serving as the reference electrode) and a polyethylene (PE) separator (16 μm thick) were used. The electrolyte solution consisted of 1 M $LiPF_6$ dissolved in a mixture of ethylene carbonate (EC) and dimethyl carbonate (DMC) in a volume ratio of 3:7. To evaluate the electrochemical performance, they were tested over various current densities within a voltage range of 0.01–1.5 V vs. Li/Li^+ (half-cells) and 2.5–4.2 V (full-cells). The initial formation stage of the cells involved charging at 0.05C followed by a discharging at 0.05C. In addition, rate capability was also evaluated by charging at varying current densities (0.2–6C), followed by discharging at 0.5C, while cycle performance was assessed under the condition of charging at 3C and discharging at 1C. Furthermore, electrochemical impedance spectroscopy (EIS) analysis was also conducted by applying a constant amplitude (5 mV) over a frequency range (1.0 MHz–0.5 mHz).

3. Results and discussion

The effectiveness of the proposed carbothermal shock process using microwave induction was primarily investigated using m-Si particles and exfoliated graphite (EG) sheets (Note S1), which is beneficial for structural tailoring and mass production of n-Si@EG composites (Figs. S1 and S2). Fig. 1a illustrates a synthesis of the n-Si@G-C composite via carbothermal shock through microwave induction. After mixing of m-Si (~4 μm) and natural graphite (~10 μm) powders in a rectangular container, carbothermal shock was applied to the mixture for 40 s by Joule heating induced by a microwave induction (Fig. S1d). The m-Si particles experienced stress fracturing through the microwave irradiation and then abundant n-Si particles were firmly attached onto the graphite surface. The fraction of n-Si particles was optimized to 10 wt%, considering the uniformity of n-Si particles on graphite to avoid undesirable particle agglomeration. In addition, we also found a small peak at $2\theta = 35.6°$, representing the formation of SiC (JCPDS 65–0360) between n-Si particles and graphite during the microwave-assisted carbothermal shock process (Fig. S3). It is expected that the formation of SiC is beneficial for ensuring stable adhesion of n-Si particles onto the graphite surface. Note that there is a noticeable growth of crystalline SiC peak in the patterns by increasing the time of microwave irradiation. Although SiC formation is crucial to ensure the adhesion of n-Si particles on the graphite surface, it is also necessary to optimize the fraction of SiC to maximize the specific capacity of the n-Si@G-C composite. In this respect, the microwave irradiation time has been optimized to 40 s in this work. The as-prepared n-Si@G-C anode allowed a good balance between reversible capacity and cycling stability (Table S1). Subsequently, a wet-coating process was employed to apply coal-tar pitch onto the resulting n-Si@G composite, followed by heating at 1000 °C. A

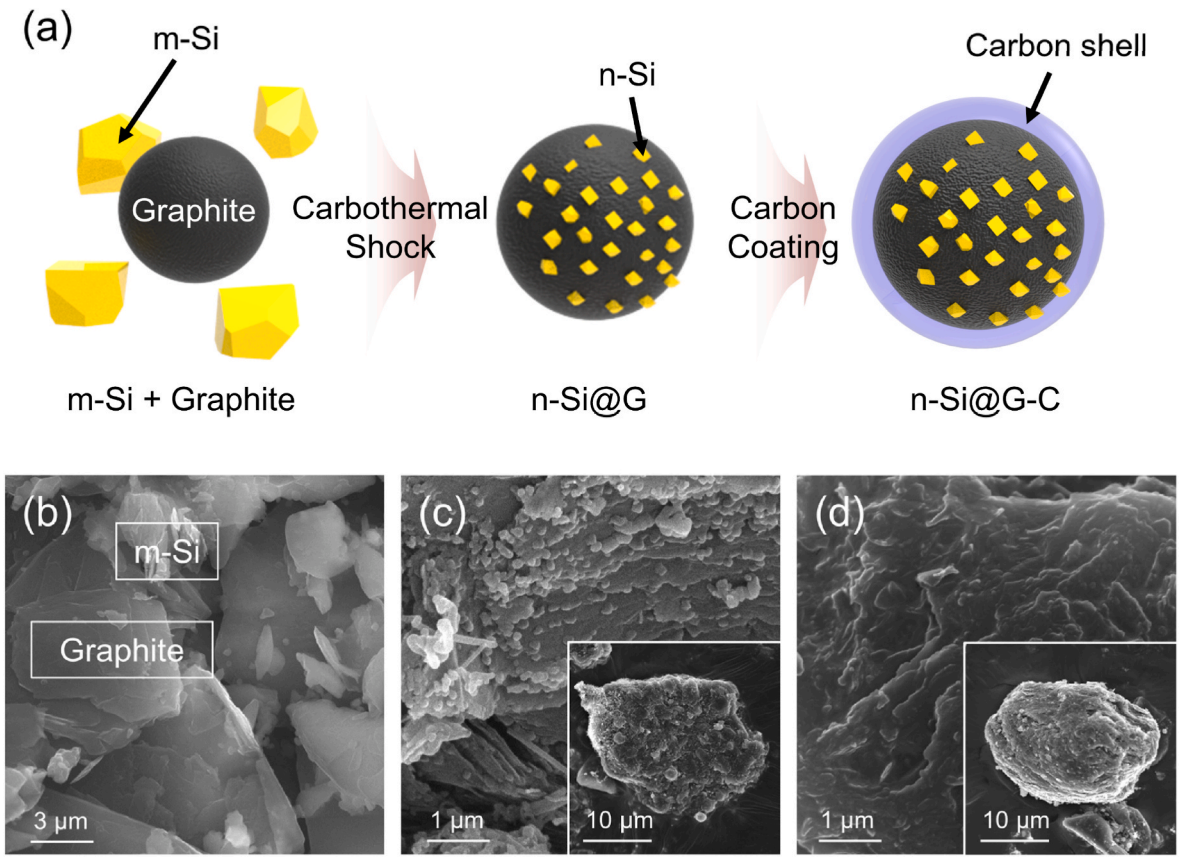

Fig. 1. (a) Synthesis process of n-Si@G-C composite by carbothermal shock through microwave induction. FESEM images of (b) a mixture of graphite and m-Si powder, (c) n-Si@G composite, and (d) n-Si@G-C composite at different magnifications.

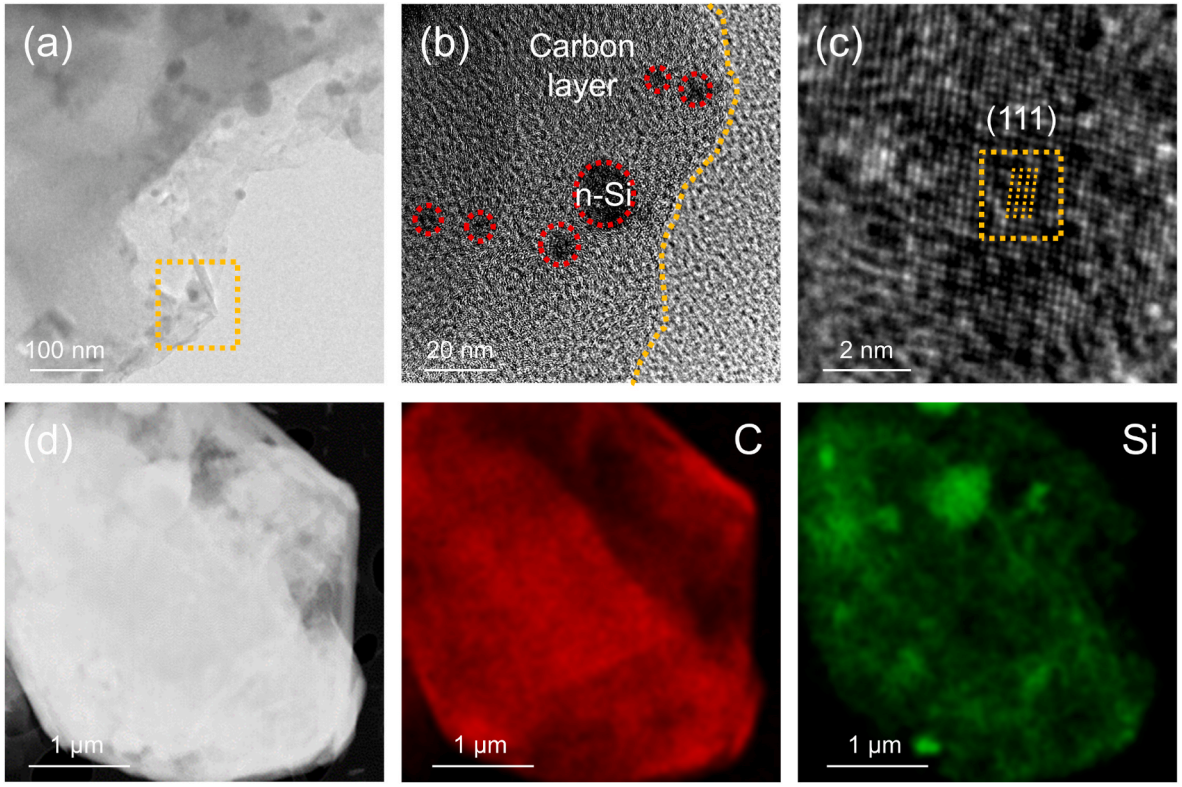

Fig. 2. (a) Bright-field TEM image and (b) HRTEM image of n-Si@G-C composite, and (c) *d*-spacing of n-Si particles anchored on the graphite surface within the n-Si@G-C composite. (d) Dark-field TEM image of n-Si@G-C composite with EDS elemental mappings for carbon (red) and silicon (green).

thin amorphous carbon shell can be formed onto the exterior of the n-Si@G composite, indicating the successful synthesis of n-Si@G-C composites covered with a durable carbon shell [26].

The morphological and microstructural investigations on the n-Si@G-C composite were thoroughly performed. In Fig. 1b, FESEM image shows a mixture of graphite and m-Si particles before the carbothermal shock process. The carbothermal shock causes a fracturing of the m-Si particles and integrates n-Si particles onto the graphite surface. The graphite particle has a roughened surface caused by the anchoring of abundant n-Si particles (~50 nm in size) in the n-Si@G composite (Fig. 1c and Fig. S4). After a subsequent surface coating with coal-tar pitch followed by heating at 1000 °C, a thin amorphous carbon shell was integrated onto the n-Si@G composite as revealed by the smooth surface morphology of the resulting n-Si@G-C composite (Fig. 1d).

A TEM observation confirmed that a thin carbon shell (~100 nm in thickness) successfully covered the n-Si@G composite, preventing external exposure of n-Si particles (Fig. 2a). A high-resolution TEM image indicates that crystalline n-Si particles (~50 nm) are integrated onto the graphite surface without agglomeration (Fig. 2b). Note that they have a *d*-spacing of 0.31 nm, representing the interplanar distance for (111) planes within Si crystals (Fig. 2c and S5) [27]. In addition, EDS elemental mappings for C (red) and Si (green) also confirmed the composition and microstructure of the n-Si@G-C composite, where n-Si particles were embedded between graphite surface and an amorphous carbon shell (Fig. 2d).

Fig. 3a compares powder XRD patterns obtained from both n-Si@G and n-Si@G-C composites, where all Braggs reflections can be indexed to the characteristic peaks of Si compounds (e.g. Si, SiO_x, SiC) and graphite. After the carbothermal shock process, the formation of an additional SiC phase was detected at 35.6° and 41.3°, maintaining the crystalline peaks of Si (27.9° and 46.8°) and graphite (26.0° and 54.1°) [27,28]. In addition, there was a small broad peak at low Braggs angle in the pattern of the n-Si@G-C composite, corresponding to the outer carbon shell (Fig. S6) [29].

In parallel, the n-Si@G-C composite was further characterized using Raman spectroscopy as depicted in Fig. 3b. The graphite matrix and amorphous carbon shell exhibited Raman spectra related to the vibrations of the E_{2g} symmetry (G-band) and the A_{1g} symmetry (D-band) at 1580 and 1350 cm^{-1}, respectively [30]. We found a noticeable increase in the intensity ratio (I_D/I_G) from 0.32 to 0.57 in the n-Si@G composite, and further to 0.78 for the n-Si@G-C composite. The higher I_D/I_G ratio, reflecting greater disorder in the carbon structures, was mainly caused by the incorporation of the amorphous carbon shell on the outer surface.

On the other hand, both n-Si@G and n-Si@G-C composites have similar particle size distributions, supporting that the carbonization process with coal-tar pitch does not experience particle agglomerations

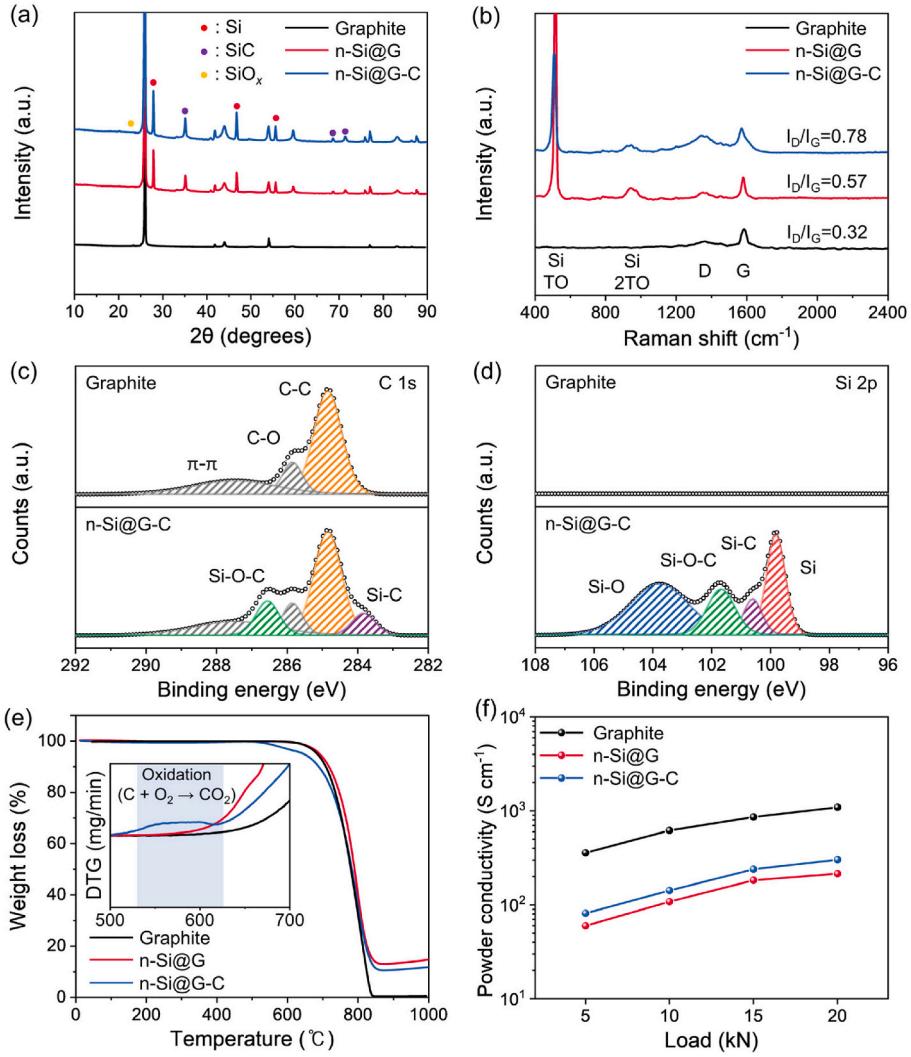

Fig. 3. (a) Powder XRD patterns and (b) Raman spectra of graphite, n-Si@G, and n-Si@G-C composites. XPS profiles of (c) C 1s and (d) Si 2p spectra for graphite and n-Si@G-C composite. (e) TGA curves of graphite, n-Si@G, and n-Si@G-C composites measured under a flow of O_2 gas with corresponding DTG profiles in the inset. (f) Electrical conductivities of graphite, n-Si@G, and n-Si@G-C composites at various applied pressures.

of the n-Si@G-C composites (Fig. S7a). From the N_2 isotherms, we found that the specific surface area of the n-Si@G-C composite is 7.0 $m^2\ g^{-1}$ with a total pore volume of 0.020 $cm^3\ g^{-1}$. These values surpass those of the n-Si@G composite, which measured at 5.9 $m^2\ g^{-1}$ and 0.015 $cm^3\ g^{-1}$, respectively. It is because the incorporation of an amorphous carbon shell onto the n-Si@G composite enlarged its surface area and total pore volume (Fig. S7b). Such increases are mainly attributed to the formation of abundant free-space inside the n-Si@G-C composite, which would be beneficial for accommodating the volume variations of n-Si particles anchored on the graphite surface within the composite. Furthermore, the tap densities of both n-Si@G and n-Si@G-C were measured at 0.85 and 0.83 g cc^{-1}, respectively, which are relatively lower than that of graphite (0.90 g cc^{-1}) due to the integration of n-Si particles and the amorphous carbon shell (Fig. S8).

To examine the chemical composition of the n-Si@G-C composite, XPS analyses were conducted. After deconvolution on the basis of C 1s excitation (284.5 eV), we thoroughly investigated the surface chemistry of the n-Si@G-C composite. In the C 1s spectra (Fig. 3c), the n-Si@G-C composite exhibited additional signals of Si–C and Si–O–C bonding at 283.8 and 286.1 eV, respectively [31], in contrast to graphite. Furthermore, it also presented notable signals for chemical bonding of Si–C (100.4 eV), Si–O–C (101.5 eV), Si–O (103.8 eV), and Si (99.8 eV) in Si 2p spectra (Fig. 3d) [32]. We suggest that additional Si–C and Si–O–C bonding would strengthen the adhesion between n-Si particles and graphite within the composite [26]. This is beneficial for preventing the separation of n-Si particles from graphite during cycling enhancing the structural integrity of n-Si particles in the composite.

The fractions of each component in the n-Si@G-C composite were confirmed by TGA analyses (Fig. 3e). The ratio of pitch-derived amorphous carbon shell and graphite in the composites observed in the derivative thermogravimetry (DTG) peaks were based on the TGA curves (in the inset). The peak observed in the low-temperature range (550–650 °C) represented the decomposition of the amorphous carbon shell, while the decomposition of graphite was ascribed to the peak observed in the high-temperature region (650–800 °C) [33]. On the other hand, the oxidation of n-Si particles induces a weight increase above 800 °C in the inset [34]. From the TGA curves, we found that the n-Si@G-C composite consists of approximately 85.1 wt% graphite, 10.4 wt% n-Si particles and 4.5 wt% amorphous carbon shell (Fig. S9). The fraction of amorphous carbon is well matched with yield (40.8 %) of the coal-tar pitch (10 wt%) during the carbonization process (Fig. S10). As presented in Fig. 3f, the electrical conductivity was measured under various applied pressures after pelletizing the composite powders. The n-Si@G-C composite exhibited superior electrical conductivity (~302.9 S cm^{-1}) than that of the n-Si@G composite (~214.8 S cm^{-1}) at a pressure of 20 kN. This shows that the introduction of the amorphous carbon shell was beneficial for enhancing the electrical conduction of the composite.

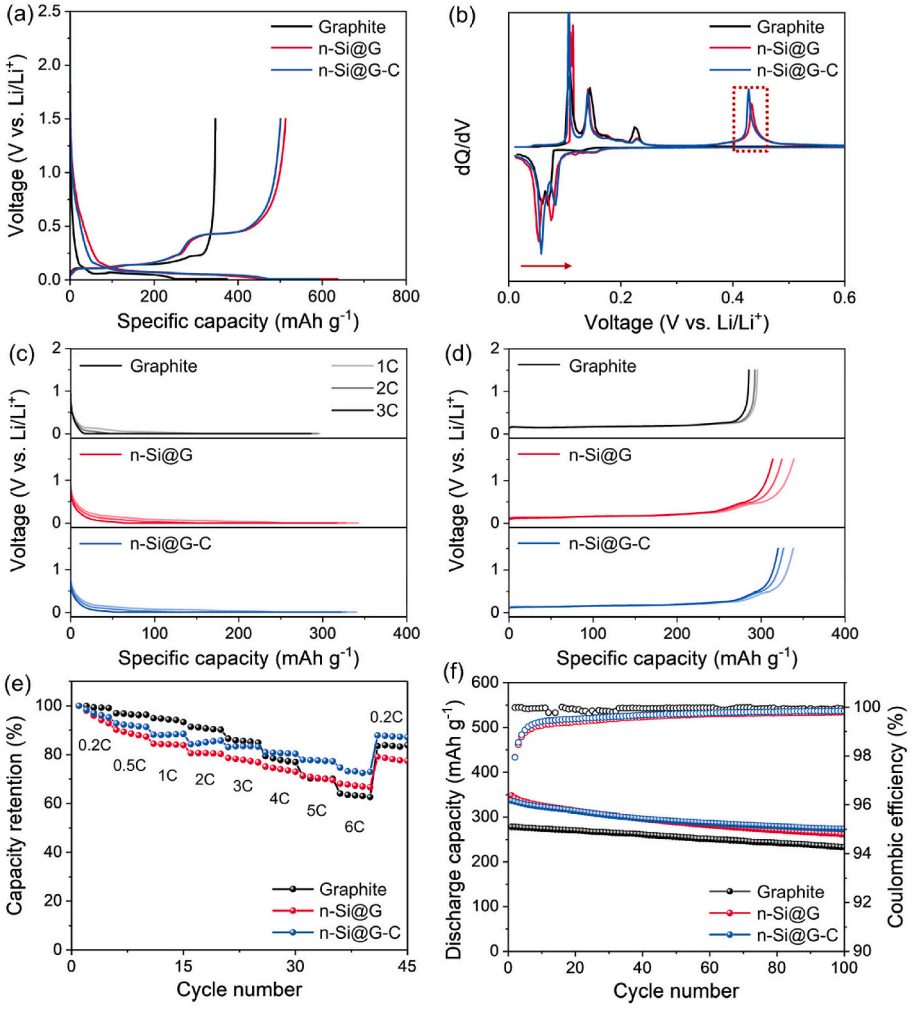

Fig. 4. Electrochemical performances of half-cells assembled with graphite, n-Si@G, and n-Si@G-C anodes: (a) galvanostatic voltage profiles recorded at a charging current density of 0.05C and (b) corresponding differential voltage (dQ/dV) profiles at the first cycle. Voltage profiles during the (c) charging and (d) discharging process at various charging current densities from 1C to 3C, constant discharging current density of 0.5C, and (e) rate capabilities at various current densities of 0.2, 0.5, 1, 2, 3, 4, 5, 6, and 0.2C. (f) Cycle performance at 3C-charging and 1C-discharging for 100 cycles.

To evaluate the electrochemical performance, galvanostatic voltage profiles of the anodes were recorded during the first cycle as compared in Fig. 4a. In comparison with the graphite anode, the n-Si@G anode exhibited a superior charge and discharge capacities of 637.2 and 513.1 mAh g^{-1}, along with an initial coulombic efficiency of 80.5 %. This enhanced reversible capacity is primarily associated with the incorporation of n-Si particles onto graphite surface within the composite as evidenced at 0.43 V vs. Li/Li^+ in the corresponding differential voltage (dQ/dV) curves (Fig. 4b). According to the dQ/dV profiles in the voltage range of 0.65–0.90 V vs. Li/Li^+, the n-Si@G-C anode exhibited a relatively smaller Li^+ consumption associated with SEI formation compared to the n-Si@G anode. It reveals that the amorphous carbon shell allows the stable SEI formation on the n-Si@G-C anode during cycling (Fig. S11). With amorphous carbon coating, the n-Si@G-C anode experienced slightly reductions in both charge capacity (594.0 mAh g^{-1}) and discharge capacity (500.8 mAh g^{-1}), yet it achieved a relatively higher coulombic efficiency (84.3 %) due to the decreased total fraction of n-Si particles within the composite. While the total charge capacity of the n-Si@G-C anode decreased, the constant current charge capacity increased with effectively reduced overpotential and charging time after the carbon coating process. It is mainly responsible for the effective conduction pathways onto the composite provided by the amorphous carbon shell and the prevention of direct electrolyte exposure of n-Si particles.

The galvanostatic voltage profiles of the anodes were compared at various charging current densities ranging from 1 to 3C (Fig. 4c), and a constant discharging current density of 0.5C (Fig. 4d). Even at a fast-charging condition of 3C, the n-Si@G-C anode exhibited superior charge and discharge capacities, compared to the graphite and n-Si@G anodes. It reveals that amorphous carbon shell suppressed undesirable side reactions of the n-Si particles in the n-Si@G-C structural configuration, contributing to enhanced reversible capacity during cycling.

The n-Si@G-C anode also demonstrated a superior rate capability, showing a strong enhancement in capacity retentions, under various current densities (0.2–6C) (Fig. 4e). In practice, the n-Si@G-C anode showed a notable capacity retention of 73.0 % at 6C, in comparison to 0.2C, while the graphite anode retained only 62.7 %. Additional comparisons of the charge capacities retention contributed by constant-current and constant-voltage charging modes are provided in Fig. S12a. The n-Si@G-C anode showed higher capacity contributions compared to the graphite anode in the CC mode over various charging current densities (1–3C). It supports that the introduction of the amorphous carbon shell allows reductions in overpotential and interfacial resistance by establishing sufficient electrical conducting pathways and suppressing direct electrolyte exposure of n-Si particles. In Fig. 4f, both n-Si@G and n-Si@G-C anodes exhibited notably higher reversible capacities than the graphite anode, showing stable cycling performance

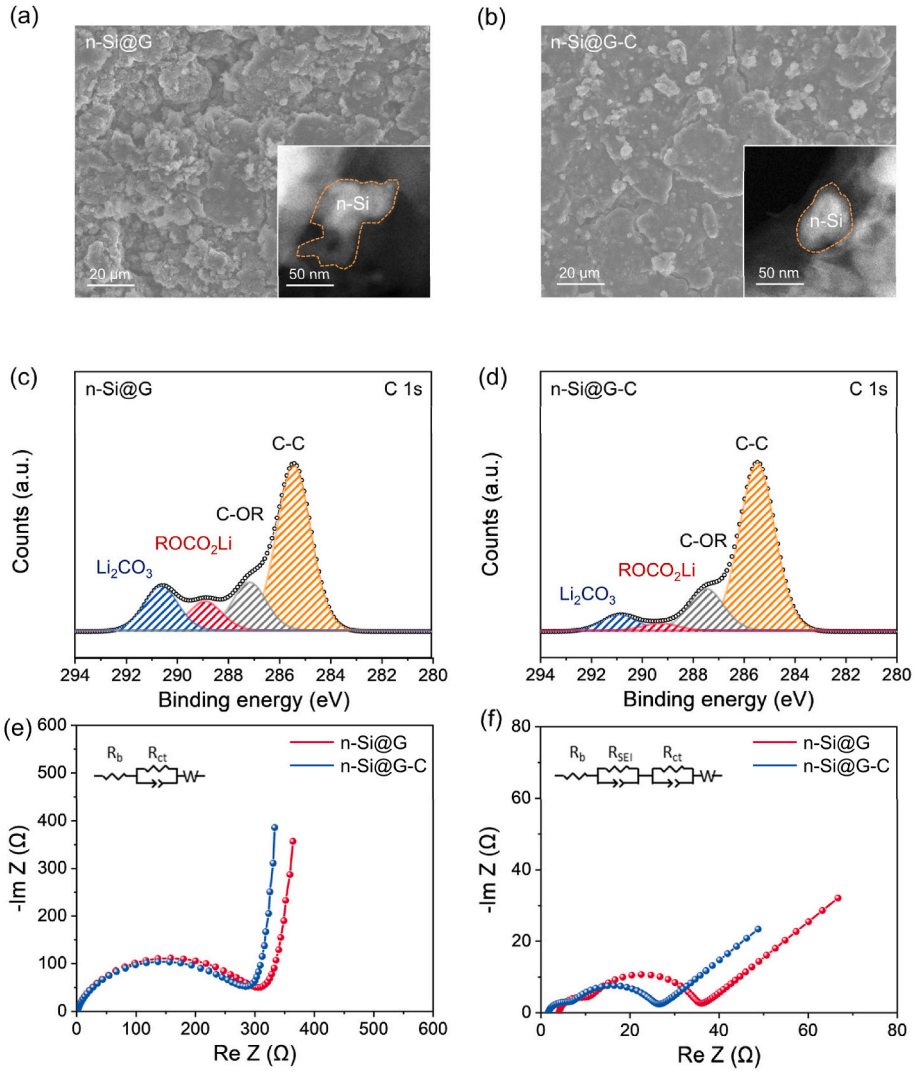

Fig. 5. Top-view FESEM images with dark-field TEM images in the inset of (a) n-Si@G and (b) n-Si@G-C anodes after 100 cycles combined with magnified images in the insets. XPS C 1s profiles of (c) n-Si@G and (d) n-Si@G-C anodes after 100 cycles. Nyquist plots of n-Si@G and n-Si@G-C anodes (e) before cycling and (f) after 100 cycles.

upon charging at 3C and discharging at 1C over 100 cycles. Note that the n-Si@G-C anodes retained more than 79.7 % of its initial capacity after cycling, while 74.9 % for the n-Si@G anode (Fig. S12b).

To support the benefits of our material design, post-mortem investigations were carefully conducted on the cycled n-Si@G and n-Si@G-C anodes. As expected, the n-Si@G anode exhibited a relatively roughened surface with the formation of microcracks because the n-Si particles were expanded, pulverized, and eventually stripped from the graphite surface after 100 cycles (Fig. 5a). The continuously exposed n-Si particles to the electrolyte facilitated additional SEI formation, leading to continuous irreversible Li^+ consumption [35]. In contrast, the n-Si@G-C anode maintained a relatively smooth surface with its initial shape allowing the uniform SEI formation (Fig. 5b). It indicates that undesirable side reactions could be effectively mitigated in the n-Si@G-C anode upon repeated cycling [36,37].

In addition, we also investigated the chemical compositions of the SEI layers on the cycled n-Si@G and n-Si@G-C anodes. From the XPS C 1s spectra, it should be noted that the SEI layer on the n-Si@G anode was mainly composed of Li_2CO_3 and $ROCO_2Li$, which are known to have an insulative nature and poor mechanical stability (Fig. 5c) [38]. In contrast, the SEI layer of the n-Si@G-C anode exhibited relatively low fractions of Li_2CO_3 and $ROCO_2Li$ after cycling (Fig. 5d). This reveals that the effective surface protection of the n-Si@G-C composite by an amorphous carbon shell suppressed the formation of insulative components (i.e. Li_2CO_3 and $ROCO_2Li$). The different chemical compositions of the SEI layers may affect the Li^+ transport in the anode thereby affecting its fast-charging capability as well as long-term cycling stability.

Fig. 5e and f displays Nyquist plots of both n-Si@G and n-Si@G-C anodes obtained before and after cycling, respectively, aiming to explain the effects of the composition of SEI layer during cycling. The plots were carefully fitted with corresponding equivalent circuit models in the insets (Table S2). Before cycling (Fig. 5e), both anodes exhibited one semicircle in the low-frequency, representing the charge-transfer resistance (R_{ct}) [39,40]. The n-Si@G-C anode has a relatively smaller value of R_{ct} (309.8 Ω) than that of the n-Si@G anode (204.6 Ω), indicating the positive effect of the conductive amorphous carbon shell on the overpotential for Li^+ transport. After cycling (Fig. 5f), we found two semi-circles corresponding to SEI resistance (R_{SEI}) in the low-frequency, and the R_{ct} in the mid-to-high-frequency. Notably, both R_{ct} and R_{SEI} values were significantly reduced in the n-Si@G-C anode by facilitating a formation of more stable SEI layer after cycling.

To further examine the feasibility of the n-Si@G-C anode, full-cells (areal capacity: 2.2 mAh cm^{-2}, N/P ratio: 1.1) assembled with a commercial-grade $LiNi_{0.8}Co_{0.1}Mn_{0.1}O_2$ cathode were cycled by galvanostatic charging at 3C and then discharging at 1C for 300 cycles. Although both full-cells exhibited similar charge capacities at 0.05C, the full-cell containing the n-Si@G-C anode showed a higher charge

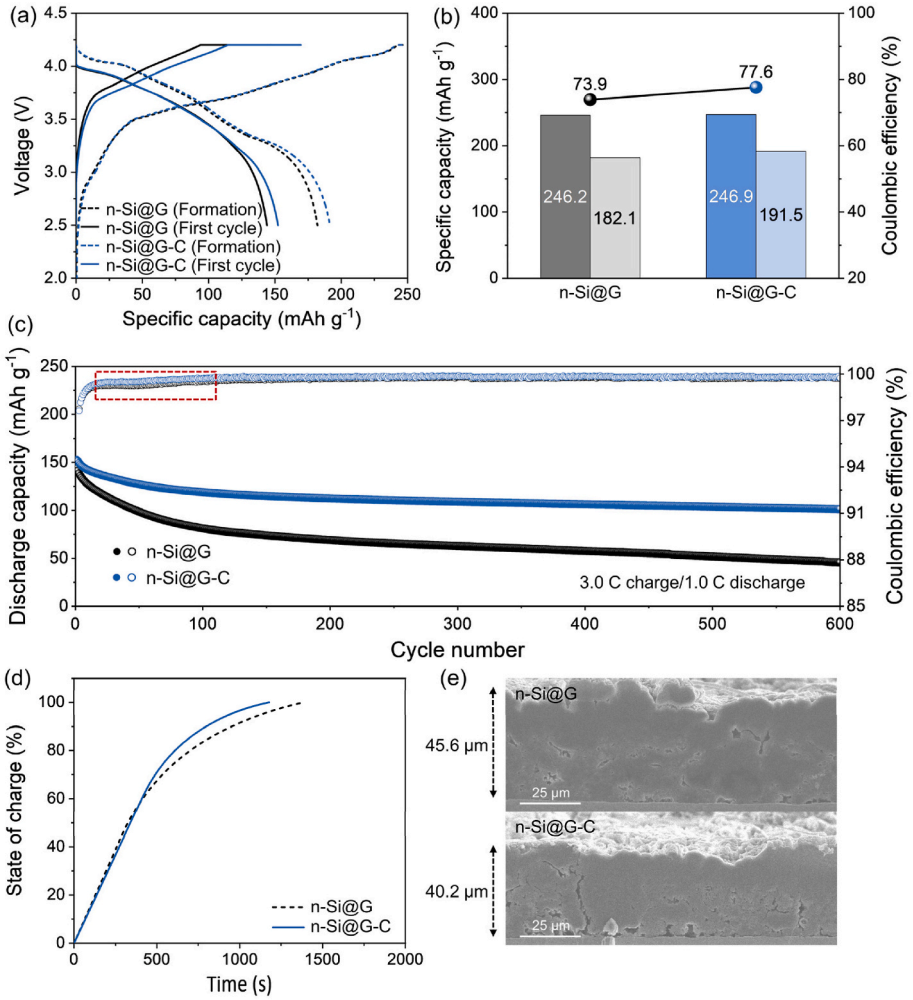

Fig. 6. Electrochemical performances of full-cells assembled with n-Si@G and n-Si@G-C anodes with an areal capacity of 2.2 mAh cm^{-2}: (a) galvanostatic voltage profiles in a voltage range of 2.5–4.2 V at selected cycles. (b) Comparisons of specific capacity and coulombic efficiency at the first cycle. (c) Cycle performance at 3C-charging and 1C-discharging over 600 cycles. (d) Charging time profiles as a function of state of charge (SOC). (e) Cross-sectional FESEM images of n-Si@G and n-Si@G-C anodes after 100 cycles in full-cells.

capacity at 3C as compared in Fig. 6a and b. This is again due to the effective protection of n-Si particles from the amorphous carbon shell which effectively enhanced the fast-charging capability of the n-Si@G-C anode.

The full-cell containing the n-Si@G anode experienced rapid capacity fading accompanied by a significant loss in coulombic efficiency during cycling, as depicted in Fig. 6c. This noticeable loss of coulombic efficiency loss was induced by the continuous formation of an unstable SEI layer throughout repeated cycling [41,42]. On the other hand, the full-cell featuring the n-Si@G-C anode demonstrated an improved reversible capacity, maintaining 71.3 % capacity retention after 300 cycles, and continued to exhibit stable performance even after 600 cycles under fast-charging conditions. Furthermore, the utilization of the n-Si@G-C anode resulted in a reduction of the charging time to 10.1 min (80 % SOC) for the full-cell (Fig. 6d). To investigate the dimensional stability, post-mortem analyses were conducted on the cycled anodes disassembled from full-cells after 100 cycles. Fig. 6e shows cross-sectional FESEM images of anodes, indicating that the thickness of n-Si@G anode was measured to be 45.6 μm while 40.2 μm for the n-Si@G-C anode after 100 cycles. These results support excessive SEI formation and volume expansion of n-Si particles could be suppressed in the n-Si@G-C anode.

4. Conclusions

We proposed a facile carbothermal shock through the utilization of π-electrons in graphite by using a tunable-voltage-current technique and microwave induction for a cost-effective and high-quality synthesis process of Si-based materials. The n-Si@G-C composite was produced through a carbothermal shock process using a mixture of m-Si and graphite powder, followed by carbon coating with coal-tar pitch. We demonstrated that the introduction of n-Si particles onto graphite surface with an amorphous carbon shell was effective for enhancing the reversible capacity and fast-charging capability. In practice, the n-Si@G-C anode exhibited a high reversible capacity (500.8 mAh g^{-1}), showing a notable capacity retention (79.7 %) after 100 cycles under the condition of charging at 3C and discharging at 1C. Moreover, the application of the n-Si@G-C anode into the full-cell was effective for reducing the charging time to 10.1 min (80 % SOC), sustaining a noticeable capacity retention (71.3 %) after 300 cycles. Such improvements are mainly attributed to the effective volume accommodation of n-Si particles and the enhancement of electrical conductivity. Our approach is a facile, scalable, and cost-effective process for the n-Si@G-C anode materials in the development of advanced LIBs.

Data availability

Data will be made available on request.

CRediT authorship contribution statement

Chang-Hyun Cho: Writing – original draft, Data curation, Conceptualization. **Won Ung Jeong:** Writing – original draft, Data curation. **Chang-Ha Lim:** Methodology, Investigation. **Jae-Kook Yoon:** Formal analysis, Data curation. **Chris Yeajoon Bon:** Writing – review & editing, Formal analysis. **Kap-Seung Yang:** Writing – original draft, Conceptualization. **Min-Sik Park:** Writing – review & editing, Supervision, Conceptualization.

Declaration of competing interest

The authors declare that they have no known competing financial interests or personal relationships that could have influenced the work reported in this paper.

Acknowledgements

This research was financially supported by the Ministry of Small and Medium-sized Enterprises (SMEs) and Startups (MSS), Korea, under the "Regional Specialized Industry Development Plus Program (R&D, S2867557)" supervised by the Korea Institute for the Advancement of Technology (KIAT).

Appendix. ASupplementary data

Supplementary data to this article can be found online at https://doi.org/10.1016/j.carbon.2024.119542.

References

[1] A. Tomazewska, Z. Chu, X. Feng, S. Okane, X. Liu, J. Chen, et al., Lithium-ion battery fast charging, A review, eTransportation 1 (2019) 100011, https://doi.org/10.1016/j.etran.2019.100011.
[2] M. Wetjen, S. Solchenbach, D. Pritzl, J. Hou, V. Tileli, H.A. Gasteiger, Morphological changes of silicon nanoparticles and the influence of cutoff potentials in silicon-graphite electrodes, J. Electrochem. Soc. 165 (2018) A1503–A1514, https://doi.org/10.1149/2.1261807jes.
[3] Y. Du, Z. Yang, Y. Yang, Y. Yang, H. Jin, G. Hou, et al., Mussel-pearl-inspired design of Si/C composite for ultrastable lithium storage anodes, J. Alloys Compd. 872 (2021) 158717, https://doi.org/10.1016/j.jallcom.2021.159717.
[4] K. Guo, R. Kumar, X. Xiao, B.W. Sheldon, H. Gao, Failure progression in the solid electrolyte interphase (SEI) on silicon electrodes, Nano Energy 68 (2020) 104257, https://doi.org/10.1016/j.nanoen.2019.104257.
[5] H. Tao, M. Huang, L. Fan, X. Qu, Effect of nitrogen on the electrochemical performance of core–shell structured Si/C nanocomposites as anode materials for Li-ion batteries, Electrochim. Acta 89 (2013) 394–399, https://doi.org/10.1016/j.electacta.2012.11.092.
[6] M.T. McDowell, I. Ryu, S.W. Lee, C. Wang, W.D. Nix, Y. Cui, Studying the kinetics of crystalline silicon nanoparticle lithiation with in situ transmission electron microscopy, Adv. Mater. 24 (2012) 6034–6041, https://doi.org/10.1002/adma.201202744.
[7] C.K. Chan, H. Peng, G. Liu, K. McIlwrath, X.F. Zhang, R.A. Huggins, et al., High-performance lithium battery anodes using silicon nanowires, Nat. Nanotechnol. 3 (2008) 31–35, https://doi.org/10.1038/nnano.2007.411.
[8] L.F. Cui, Y. Yang, C.M. Hsu, Y. Cui, Carbon−Silicon Core−Shell nanowires as high capacity electrode for lithium ion batteries, Nano Lett. 9 (2009) 3370–3374, https://doi.org/10.1021/nl901670t.
[9] H. Wu, G. Chan, J.W. Choi, I. Ryu, Y. Yao, M.T. McDowell, et al., Stable cycling of double-walled silicon nanotube battery anodes through solid–electrolyte interphase control, Nat. Nanotechnol. 7 (2012) 310–315, https://doi.org/10.1038/nnano.2012.35.
[10] N. Liu, H. Wu, M.T. McDowell, Y. Yao, C. Wang, Y. Cui, A yolk-shell design for stabilized and scalable Li-ion battery alloy anodes, Nano Lett. 12 (2012) 3315–3321, https://doi.org/10.1021/nl3014814.
[11] H. Wu, G. Yu, L. Pan, N. Liu, M.T. McDowell, Z. Bao, et al., Stable Li-ion battery anodes by in-situ polymerization of conducting hydrogel to conformally coat silicon nanoparticles, Nat. Commun. 4 (2013) 1943, https://doi.org/10.1038/ncomms2941.
[12] C. Wang, H. Wu, Z. Chen, M.T. McDowell, Y. Cui, Z. Bao, Self-healing chemistry enables the stable operation of silicon microparticle anodes for high-energy lithium-ion batteries, Nat. Chem. 5 (2013) 1042–1048, https://doi.org/10.1038/nchem.1802.
[13] N. Liu, Z. Lu, J. Zhao, M.T. McDowell, H.W. Lee, W. Zhao, et al., A pomegranate-inspired nanoscale design for large-volume-change lithium battery anodes, Nat. Nanotechnol. 9 (2014) 187–192, https://doi.org/10.1038/nnano.2014.6.
[14] Y. Li, K. Yan, H.W. Lee, Z. Lu, N. Liu, Y. Cui, Growth of conformal graphene cages on micrometre-sized silicon particles as stable battery anodes, Nat. Energy 1 (2016) 15029, https://doi.org/10.1038/nenergy.2015.29.
[15] W. Liu, H. Xu, H. Qin, Y. Lv, F. Wang, G. Zhu, et al., The effect of carbon coating on graphite@nano-Si composite as anode materials for Li-ion batteries, J. Solid State Electrochem. 23 (2019) 3363–3372, https://doi.org/10.1007/s10008-019-04413-3.
[16] B. Liu, P. Huang, Z. Xie, Q. Huang, Large-scale production of a silicon nanowire/graphite composites anode via the CVD method for high-performance lithium-ion batteries, Energy Fuels 35 (2021) 2758–2765, https://doi.org/10.1021/acs.energyfuels.0c03725.
[17] T. Kasukabe, H. Nishihara, K. Kimura, T. Matsumoto, H. Kobayashi, M. Okai, et al., Beads-milling of waste Si sawdust into high-performance nanoflakes for lithium-ion batteries, Sci. Rep. 7 (2017) 42734, https://doi.org/10.1038/srep42734.
[18] C.K. Dixit, S. Bhakta, A. Kumar, S.L. Suib, J.F. Ruling, Fast nucleation for silica nanoparticle synthesis using a sol–gel method, Nanoscale 8 (2016) 19662–19667, https://doi.org/10.1039/C6NR07568A.
[19] Y. Yao, Z. Huang, P. Xie, S.D. Lacey, R.J. Jacob, H. Xie, et al., Carbothermal shock synthesis of high-entropy-alloy nanoparticles, Science 30 (2018) 1489–1494, https://doi.org/10.1126/science.aan5412.

[20] C.H. Cho, C.S. Woo, K.S. Yang, C.H. Lim, C.H. Joh, Method of manufacturing composite anode material and composite anode material for lithium secondary battery, US Patent No. US 11 (2022) 367–865, filed Nov. 18, 2019, issued Jun. 21.
[21] C.H. Kim, M.S. Kim, Y.A. Kim, K.S. Yang, S.J. Baek, Y.J. Lee, et al., Electroconductively deposited carbon fibers for power controllable heating elements, RCS Adv 5 (2015) 26998–27002, https://doi.org/10.1039/c5ra01296a.
[22] K.S. Yang, Y.J. Yoon, M.S. Lee, W.J. Lee, J.H. Kim, Further carbonization of anisotropic and isotropic pitch-based carbons by microwave irradiation, Carbon 40 (2002) 897–903, https://doi.org/10.1016/S0008-6223(01)00210-X.
[23] D.W. Kim, K.K. Im, H.J. Kim, D.H. Lee, Y.A. Kim, J. Choi, et al., Effects of electromagnetic irradiation on low-molecular-weight fraction of fluidized catalytic cracking decant oil for synthesis of pitch precursor, J. Ind. Eng. Chem. 82 (2020) 205–210, https://doi.org/10.1016/j.jiec.2019.10.014.
[24] T. Kim, J. Lee, K.H. Lee, Microwave heating of carbon-based solid materials, Carbon Lett 15 (2014) 15–24, https://doi.org/10.5714/CL.2014.15.1.015.
[25] M. Hotta, M. Hayashi, M.T. Lanagan, D.K. Argawal, K. Nagata, Complex permittivity of graphite, carbon black and coal powders in the ranges of X-band frequencies (8.2 to 12.4 GHz) and between 1 and 10 GHz, ISIJ Int. 51 (2011) 1766–1772, https://doi.org/10.2355/isijinternational.51.1766.
[26] Y. Liu, X. Liu, Y. Zhu, J. Wang, W. Ji, X. Liu, Scalable synthesis of pitch-coated nanoporous Si/graphite composite anodes for lithium-ion batteries, Energy Fuels 37 (6) (2023) 4624–4631, https://doi.org/10.1021/acs.energyfuels.2c03702.
[27] Zhou, Y. Yin, A. Cao, L. Wan, Y. Guo, Efficient 3D conducting networks built by graphene sheets and carbon nanoparticles for high-performance silicon anode, ACS Appl. Mater. Interfaces 4 (5) (2012) 2824–2828, https://doi.org/10.1021/am3005576.
[28] R.J. Iwanowski, K. Fronc, W. Paszkowicz, M. Heinonen, XPS and XRD study of crystalline 3C-SiC grown by sublimation method, J. Alloys Compd. 286 (1999) 143–147, https://doi.org/10.1016/S0925-8388(98)00994-3.
[29] P. Lu, Y. Sun, H. Xiang, X. Liang, Y. Yu, 3D amorphous carbon with controlled porous and disordered structures as a high-rate anode material for sodium-ion batteries, Adv. Energy Mater. 8 (8) (2018) 1702434, https://doi.org/10.1002/aenm.201702434.
[30] G. Velpula, R. Phillipson, J.X. Lian, D. Cornil, P. Walke, K. Verguts, et al., Graphene meets ionic liquids: fermi level engineering via electrostatic forces, ACS Nano 13 (3) (2019) 3512–3521, https://doi.org/10.1021/acsnano.8b09768.
[31] P. Uznanski, A.W. Pietrzykowska, K. Jankowski, J. Zakrzewska, A.M. Wrobel, J. Balcerzak, et al., Atomic hydrogen induced chemical vapor deposition of silicon oxycarbide thin films derived from diethoxymethylsilane precursor, Appl. Organomet. Chem. 34 (8) (2020) e5674, https://doi.org/10.1002/aoc.5674.
[32] S.Y. Kim, J. Lee, B.H. Kim, Y.-J. Kim, K.S. Yang, M.-S. Park, Facile synthesis of carbon-coated silicon/graphite spherical composites for high-performance lithium-ion batteries, ACS Appl. Mater. Interfaces 8 (19) (2016) 12109–12117, https://doi.org/10.1021/acsami.5b11628.
[33] I.-T. Kim, J. Lee, J.-C. An, E. Jung, H.-K. Lee, M. Morita, et al., Capacity improvement of tin-deposited on carbon-coated graphite anode for rechargeable lithium ion batteries, Int. J. Electrochem. Sci. 11 (7) (2016) 5807–5818.
[34] R. Patil, M. Phadatare, N. Blomquist, J. Örtegren, M. Hummelgård, J. Meshram, et al., Highly stable cycling of silicon-nanographite aerogel-based anode for lithium-ion batteries, ACS Omega 6 (10) (2021) 6600–6606, https://doi.org/10.1021/acsomega.0c05214.
[35] S.J. An, J. Li, C. Daniel, D. Mohanty, S. Nagpure, D. L. W. III, The state of understanding of the lithium-ion-battery graphite solid electrolyte interphase (SEI) and its relationship to formation cycling, Carbon 105 (2016) 52–76, https://doi.org/10.1016/j.carbon.2016.04.008.
[36] E. Moyassari, L. Streck, N. Paul, M. Trunk, R. Neagu, C.-C. Chang, et al., Impact of silicon content within silicon-graphite anodes on performance and Li concentration profiles of Li-ion cells using neutron depth profiling, J. Electrochem. Soc. 168 (2021) 020519, https://doi.org/10.1149/1945-7111/abe1db.
[37] X. Zhao, V.-P. Lehto, Challenges and prospects of nanosized silicon anodes in lithium-ion batteries, Nanotechnology 32 (2021) 042002, https://doi.org/10.1088/1361-6528/abb850.
[38] Q. Zhang, J. Pan, P. Lu, Z. Liu, M.W. Verbrugge, B.W. Sheldon, et al., Synergetic effects of inorganic components in solid electrolyte interphase on high cycle efficiency of lithium ion batteries, Nano Lett. 16 (3) (2016) 2011–2016, https://doi.org/10.1021/acs.nanolett.5b05283.
[39] W. Choi, H.-C. Shin, J.M. Kim, J.-Y. Choi, W.-S. Yoon, Modeling and applications of electrochemical impedance spectroscopy (EIS) for lithium-ion batteries, J. Electrochem. Sci. Technol. 11 (1) (2020) 1–13, https://doi.org/10.33961/jecst.2019.00528.
[40] D. Aurbach, M.D. Levi, E. Levi, A review on the solid-state ionics of electrochemical intercalation processes: how to interpret properly their electrochemical response, Solid State Ionics 179 (2008) 742–751, https://doi.org/10.1016/j.ssi.2007.12.070.
[41] H. Sun, G. Xin, T. Hu, M. Yu, D. Shao, X. Sun, et al., High-rate lithiation-induced reactivation of mesoporous hollow spheres for long-lived lithium-ion batteries, Nat. Commun. 5 (2014) 4526, https://doi.org/10.1038/ncomms5526.
[42] E. Moyassari, T. Roth, S. Kücher, C.-C. Chang, S.-C. Hou, F.B. Spingler, et al., The role of silicon in silicon-graphite composite electrodes regarding specific capacity, cycle stability, and expansion, J. Electrochem. Soc. 169 (2022) 010504, https://doi.org/10.1149/1945-7111/ac4545.